Materials Chemistry and Physics 203 (2018) 223–234

Contents lists available at ScienceDirect

Materials Chemistry and Physics

journal homepage: www.elsevier.com/locate/matchemphys

Surface modification of rice-husk ash (RHA) by Si_3N_4 coating to promote its wetting by Al-Mg-Si alloys

Niloofar Soltani [a, b, *, 1], Amin Bahrami [a, b, 1], Martin I. Pech-Canul [b], Luis A. González [b], Aleksander Gurlo [c]

[a] Instituto de Investigaciones en Materiales, Universidad Nacional Autónoma de México, Ciudad Universitaria, 04510 D.F., Mexico
[b] Centro de Investigación y de Estudios Avanzados del Instituto Politécnico Nacional, Cinvestav-Saltillo. Av, Industria Metalúrgica No. 1062, Parque Industrial Saltillo-Ramos Arizpe, Ramos Arizpe, Coahuila, 25900, Mexico
[c] Fachgebiet Keramische Werkstoffe, Institut füfr Werkstoffwissenschaften und−technologien, Fakultät III Prozesswissenschaften, Technische Universität Berlin, Hardenbergstraße 40, Berlin, 10623, Germany

HIGHLIGHTS

- A three-step study was done to enhance wettability of RHA by Al-Mg-Si alloys.
- Si_3N_4 coated on RHA by hybrid CVI system, using solid precursor of Na_2SiF_6.
- Optimum processing parameters to maximize the amount of deposited Si_3N_4 were defined.
- By coating RHA with Si_3N_4 the contact angle decreased from 72° to 35°.

GRAPHICAL ABSTRACT

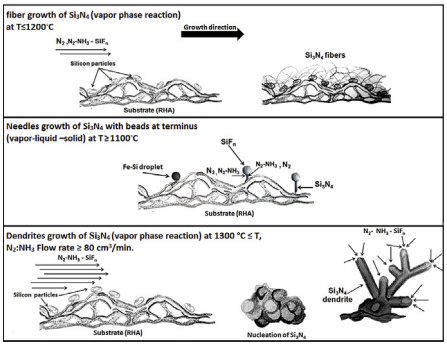

ARTICLE INFO

Article history:
Received 23 November 2016
Received in revised form
19 September 2017
Accepted 6 October 2017
Available online 8 October 2017

Keywords:
Na_2SiF_6 decomposition
Chemical vapor infiltration
Rice-husk ash
Wettability
Surface modification

ABSTRACT

Success in the manufacture by the liquid-state route of Al-matrix composites reinforced with RHA strongly depends upon its suitable wetting by the aluminum alloys. Since RHA is scarcely wetted by Al alloys, development of appropriate wetting technologies is paramount. A three-step investigation has been conducted to enhance wettability of RHA by two Al-Mg-Si alloys. In the first step, a study on the coating of RHA with Si_3N_4 by the hybrid system chemical vapor infiltration using Na_2SiF_6 solid precursor and N_2 and N_2-NH_3 as gas precursors, was conducted. The second step consisted of studying the quantitative effect of processing parameters to maximize the amount of Si_3N_4 deposited into porous silica preforms. In the third stage, a wettability study using the sessile drop method was conducted to elucidate the effect of Si_3N_4 coating by comparing the wetting behavior by two Al alloys of RHA substrates, reagent-grade Si_3N_4 and Si_3N_4-coated RHA substrates.

1. Introduction

The low electrical conductivity, low thermal expansion coefficient and density of SiO_2 when compared to SiC and B_4C, makes it

* Corresponding author. Instituto de Investigaciones en Materiales, Universidad Nacional Autónoma de México, Ciudad Universitaria, 04510 D.F., Mexico.
E-mail address: niloofar.soltani@iim.unam.mx (N. Soltani).
[1] Contributed equality.

https://doi.org/10.1016/j.matchemphys.2017.10.009
0254-0584/

an appealing prospective reinforcement for metal matrix composites [1–4]. Owing to its unique natural structure – while having silica as a major constituent –, rice husk ash (RHA) has the potential to be a value-added recycling material for use as silica monoliths, reinforcement and functionality phase in metal and ceramic matrix composites [5–8]. Nonetheless, as an oxide material, the wettability of RHA by molten aluminum alloys is poor [9–11]. One alternative for overcoming the wettability issue is by engineering coatings on RHA with materials that improve wetting, protect the reinforcement from attack by liquid aluminum or enhance the matrix/reinforcement interface strength. It has been reported that low contact angles are observed in aluminum alloys in contact with silicon nitride (Si_3N_4), making it a promising material for coating RHA [9,12]. In addition, Si_3N_4 has a low impurity incorporation, low self-diffusion coefficient, good thermal conductivity and good resistance to high temperature. For these reasons, recently Si_3N_4 has caught the attention of several technological and industrial fields, including microelectronics and optoelectronics [13,14].

The production of silicon nitride powders with different purity, morphology and sintering activity lies essentially in four synthesis routes: (a) the direct reaction of elemental silicon with nitrogen gives place generally to coarse products which have to be milled prior to further processing [15]; (b) carbothermal reduction, which utilizes fine mixture of SiO_2 and carbon powders in nitrogen atmosphere at 1500 °C [16]; the diimide-process, which uses liquid or gas-phase precursors [17]; (d) CVD techniques, which use volatile silicon compounds such as $SiCl_4$, SiH_4 or related molecular compounds by reaction with ammonia [18,19]. Silicon nitride films with a large number of hydrogen radicals incorporated in its structure are produced when using silane by CVD (SiH_4) [20]. The -SiH radicals may act as charge traps in the silicon nitride [21,22] and produce a great instability in the electric characteristics of the devices.

In this regard, some attempts have been made to reduce the presence of those radicals. In presence of fluorine source, it seems that the fluorine atoms can substitute the hydrogen atoms linked to silicon atoms, forming Si-F bonds with a higher bonding energy (536 kJ mo1^{-1}) than the Si-H bonding energy (295 kJ mol^{-1}) [23]. In addition, fluorine atoms saturate the extra silicon dangling bonds in the film, which prevent the formation of traps in the nitride and also decrease the surface state density. Kinetics of Si_3N_4 film depositions from various gaseous systems with ammonia shows that kinetic constant for formation of Si_3N_4 at normal pressure deposition systems increase in the order K $SiC1_4$< K SiH_2Cl_2 < $KSiH_4$. The fact that silane is more thermally unstable than $SiCl_4$, while SiH_2C1_2 shows an intermediate stability, explains this tendency. The lowest activation energy is for SiH_4 whilst the highest one is for $SiCl_4$, keeping SiH_2C1_2 as the precursor with an intermediate value [24].

In this contribution, the hybrid system chemical vapor deposition and infiltration (HYSY-CVD and HYSY-CVI) methods were used [25]. In order to promote wetting of RHA by two Al alloys, a threefold objective has been established for this investigation. The first objective consisted of depositing Si_3N_4 on RHA, via the thermal decomposition of Na_2SiF_6 in nitrogen containing atmospheres. The second objective was to establish the optimum processing conditions for maximizing the amount of silicon nitride deposited into porous silica (RHA) preforms by studying the quantitative effect of time and temperature, gas flow rate and nitrogen precursor (N_2 or N_2-5 vol. % NH_3) on the amount of Si_3N_4 formed. Using the sessile drop method, the third objective was to conduct a comparative study of the wetting of Si_3N_4 coated silica, reagent-grade Si_3N_4 and SiO_2 (RHA) substrates with two experimental Al-Si-Mg alloys, with the final aim of optimizing the wetting conditions.

2. Experimental

2.1. Materials and preform preparation

Depending on the type of chemical or thermal treatment, amorphous or different types of crystalline silica can be obtained from rice husk (RH) [9,26]. In this study rice husk was washed with water to remove dirt and other contaminants and then was dried in open air for one day. The washed and dried rice husks was calcined at 950 °C for 2 h in a muffle furnace and air atmosphere. A representative X-ray diffraction pattern of silica obtained is shown in Fig. 1 [27]. Using the aforementioned method of incineration, tridymite and cristobalite phases were detected in the XRD patterns.

Cylindrical preforms (1 cm diameter × 0.5 cm height) with 50% porosity were prepared by uniaxial compaction of SiO_2(RHA)/Si with 10 wt % Si (Spectrum Chemical Mfg. Corp. New Brunswick, NJ, USA). Likewise, cylindrical compacts (3.175 cm in diameter × 1 cm long) were prepared using an amount of 15 g of sodium hexafluorosilicate (Na_2SiF_6, Merck, Germany).

2.2. Materials and substrate preparation

Disk-shaped SiO_2, Si_3N_4 (3 cm in diameter × 0.5 cm thick) were prepared by the compaction (pressure ≈ 35 MPa) of the corresponding materials. For preparation of Si_3N_4-coated silica, substrates were processed in a hybrid system chemical vapor infiltration (CVI) reactor.

2.3. Processing of SiO_2/Si_3N_4 porous preforms via HYSY-CVI

The porous preforms were processed in a hybrid system chemical vapor infiltration (HYSY-CVI) reactor, which consists of a horizontal tube furnace equipped with devices to control the type of nitrogen precursor as well as its flow rate. In order to make it an environmentally-friendly system, it also includes a powder collector and a neutralizer of the gas by-products. The SiO_2/Si porous preforms were consistently placed in the center of the reactor and the Na_2SiF_6 compacts were located in a low temperature zone between the gas entrance and porous preform (see Fig. 2). The prearranged positioning of the Na_2SiF_6 compact allows controlling the decomposition rate of it in the temperature range under study. Under the type of nitrogen atmosphere (N_2 or N_2-5% NH_3), the

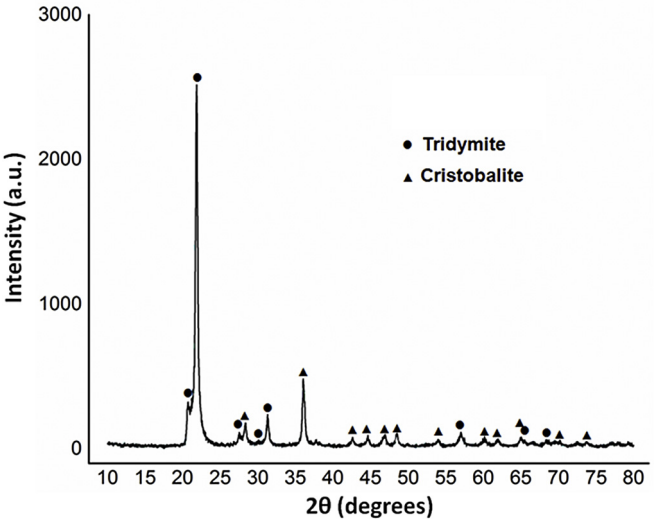

Fig. 1. X-ray diffraction pattern of silica produced from RH treated at 950 °C.

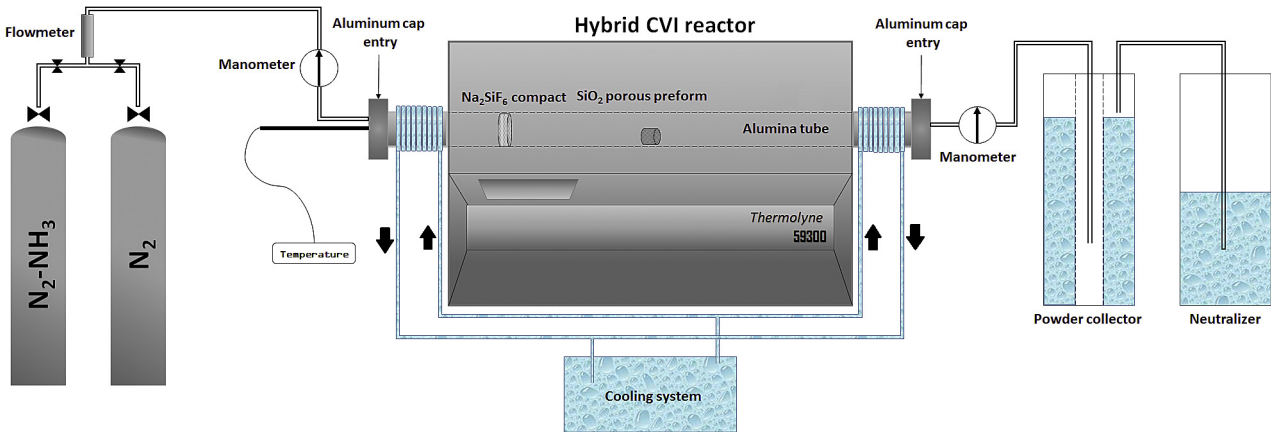

Fig. 2. Schematic representation of the experimental set-up.

system was heated at a constant rate of 20 °C/min up to the test temperature, held isothermally during the established test time and cooled down to room temperature, maintaining the same atmosphere. DTA/TG, analyses were performed at atmospheric pressure in nitrogen on a *SDT Q600* (*V20.9 Build 20*) apparatus at heating rate of 20 °C min^{-1}. Phase analyses of the final products were performed using CuKα radiation in a Philips 3040 X-ray diffractometer. The microstructure of the samples after deposition was examined in a scanning electron microscope (SEM) provided with an energy dispersive X-ray (EDX) analyzer. Thermodynamic calculations on the feasibility of the reactions involved in the $Na_2SiF_{6(s)}$-$NH_{3(g)}$-$N_{2(g)}$ system by CVI were carried out using the FactSage™ software and databases. The three-dimensional structure of the preform before and after processing was analyzed by using a Hamamatsu microfocus X-ray source and flat panel sensor. The voxel size of the obtained reconstructed volume was 7 μm. The volume was visualized by VGStudio MAX 2.2.

2.4. Optimization of process parameters for coating RHA with Si_3N_4

In order to determine the quantitative effect of the processing parameters on the total amount of deposited phases, analysis of variance (ANOVA) was performed. An L_9 Taguchi experimental design was used to study the effect of the following processing parameters in two and three levels on the deposition of Si_3N_4 by HYSY-CVI: nitrogen precursor (N_2, and 5 vol% NH_3-balance N_2), nitrogen precursor flow rate (20, 60, and 100 cm^3min^{-1}), time (45, 60, and 90 min) and temperature (1100, 1200 and 1300 °C). Table 1 shows the L_9 orthogonal array used for optimizing the Si_3N_4 coating on SiO_2.

2.5. Wettability study

The wettability behavior of Si_3N_4, SiO_2 (RHA) and CVD-Si_3N_4 on silica substrates by two different Al-Mg-Si alloys was investigated by the sessile drop method. Aluminum specimens – ~10×10×10 mm in size – were cut from as-cast aluminum alloys, polished and cleaned ultrasonically in acetone before placing them on the top of the substrates. Sessile drop tests were performed in ultra-high-purity (UHP) Ar and N_2 (O_2 traces < 5 ppm) by heating the metal/substrate specimens at a rate of 15 °C/min up to the test temperature in a tube furnace provided with an optical window, enabling the sessile drop on the substrate to be illuminated and projected onto a screen. Contact angles were measured directly from the images of the droplet profiles with an accuracy of ±2°.

3. Results and discussion

3.1. Thermodynamic evaluation of Na_2SiF_6-N_2-NH_3 reaction system

Sodium hexafluorosilicate starts to decompose at relatively low temperatures (<600 °C) [28]. Fig. 3a presents the TGA–DTA curves of the decomposition of Na_2SiF_6. The TGA curve shows just one stage of weight loss. At this stage (128.66–573.29 °C, weight loss = 98.6%), one endothermic peak at 570.87 °C in the DTA curve, which comes from the decomposition of Na_2SiF_6 was observed. Equilibrium thermodynamic predictions of Na_2SiF_6 show that, although SiF_4 is the main product of Na_2SiF_6 decomposition, there are three minor products, namely, SiF_3, SiF_2, and SiF. Fig. 3b shows plots of log Mol_{SiF_n} of decomposed Na_2SiF_6 vs. temperature in the reactor.

Table 1
Orthogonal array L_9 used for optimizing Si_3N_4 coating on SiO_2.

Trial/Run	Temperature (°C)	Time (min)	Flow rate (cm^3/min)	Atmosphere (N_2–NH_3)
1	1300	90	100	95:5
2	1300	60	60	100:0
3	1300	45	20	95:5
4	1200	90	100	95:5
5	1200	60	60	95:5
6	1200	45	20	100:0
7	1100	90	100	100:0
8	1100	60	60	95:5
9	1100	45	20	95:5

Constant parameters: Amount of Na_2SiF_6 = 15 g, Porosity of the preform = 50%.
System total pressure = (15 mbar), Heating and cooling rate = 20 °C/min.

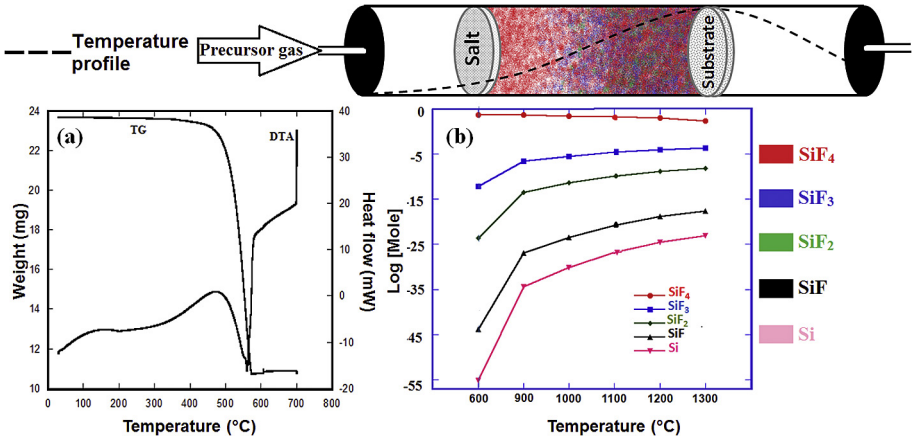

Fig. 3. a) Thermal analysis of Na_2SiF_6 by DTA/TG, and b) Equilibrium logarithm of the silicon gas species (SiF_n) formed from Na_2SiF_6.

As it can be interpreted from Fig. 3 the only gas species that presents a high partial pressure is SiF_4, due to its high thermal stability over the temperature range of 600–1300 °C. Although, increment in temperature results in higher mole production of $SiF_{n\leq 3}$ gases in the system, this enhancement is not significant. Based on data from previous work, the dissociative chemisorption on silicon is a rational process to enhance reduction of the SiF_4 molecules to the more active SiF_n and prompt SiF_4 volatilization. By this process SiF_4 loses one or more F atoms by attack of Si-Si bond with strength of the order of 80 kJ/mol by diffusing F atoms [23,29–31].

Further, by increasing temperature the possibility of reactions of SiF_4 with Si increases, and therefore the partial pressures of the other species increase.

$$SiF_4(g) + Si \rightarrow 2SiF_2(g) \quad \Delta G_{1300} = -100 kJ/mol \tag{1}$$

$$SiF_4(g) + SiF_2(g) \rightarrow 2SiF_3(g) \quad \Delta G_{1300} = -8.4 kJ/mol \tag{2}$$

3.2. The condensed-phase distribution at different temperatures

To illustrate more clearly the correlation among the production of Si_3N_4 and temperature, the conditions of the thermodynamic stability diagrams are fixed at P = 1 atm. As it can be seen in Fig. 4, at 1300 °C the condensed phase products include two regions for the system SiF_n–N_2-NH_3 (n = 0, 1, 2, 3): Si_3N_4+ non-condensed phase (NCP), Si_3N_4+ Si+(NCP), which vary with the molar ratios of mixture gases, and include two regions for the system SiF_4-NH_3-N_2: NCP, NCP + Si_3N_4.

By decreasing the temperature in system "SiF_n (n = 0, 1, 2, 3)-N_2-NH_3" region II including Si_3N_4 as condensed phase decreases. However, in the case of SiF_4 as reactant gas, it has an opposite effect. At the same time, another important feature to be noted is the region of co-deposition of Si + Si_3N_4+NCP and Si_3N_4+NCP phase, which is affected by the reactive gases. By increasing the F:Si ratio up to 3, the region of Si_3N_4 increases. The feasibility of these reactions can be related to dissociation energy values of SiF_n species and N_2 and NH_3 as reactive gases. The neutral bond dissociation energies for SiF_4, SiF_3, SiF_2, and SiF are 6.94, 5.33, 6.75 and 5.64 eV, respectively [32]. It can be seen that SiF_3 requires less energy while SiF_4 more energy to dissociate than the other species. Thus, SiF_3 has

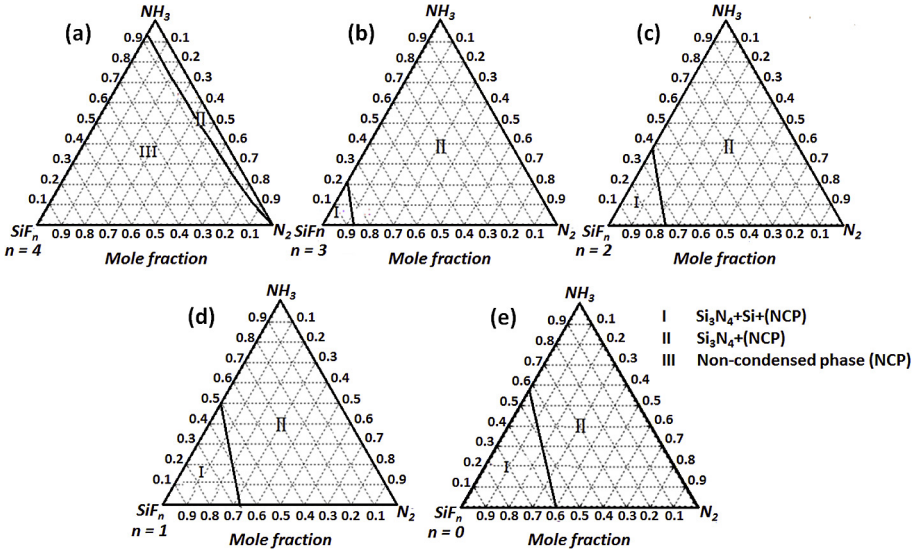

Fig. 4. Thermodynamic stability diagrams for system of "SiF_n-NH_3-N_2" at 1300 °C, P = 1 atm for a) n = 4, b) n = 3, c) n = 2, d) n = 1, and e) n = 0.

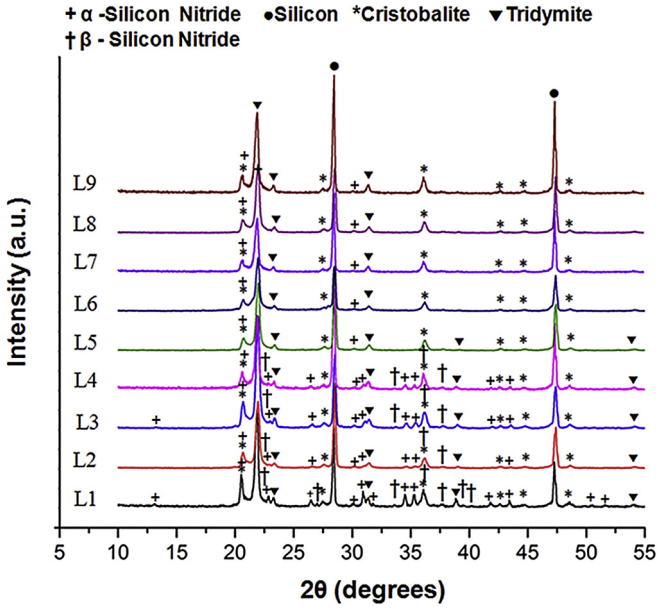

Fig. 5. X-ray diffraction patterns for all test specimens in the 2θ range 5–55°.

the highest inclination to participate in the chemical reactions in comparison with the other species. The lower dissociation energy and higher partial pressure of SiF_3 than other species ($SiF_n \leq 2$) at 1300 °C in the system, makes it the most active participant in the reaction for Si_3N_4 formation. In comparison to the other species, the widest area of co-deposition of Si_3N_4 (zone II in Fig. 4b) can be obtained by utilization of SiF_3. By increasing the n value in SiF_n to 4, due to less reactivity of SiF_4, Si_3N_4 region would not be as wide as it is with other species.

3.3. Phase analysis

3.3.1. X-ray diffraction

Results from the analysis by X-ray diffraction of all test specimens (L_1–L_9) are shown in Fig. 5 from 5 to 55° 2θ degrees for all identified phases. Depending on the experimental conditions α-Si_3N_4 (JCPDS Card No. 73–1210) and β-Si_3N_4 (JCPDS Card No. 71–0453) are formed in different proportions. Cristobalite (JCPDS Card No. 77–1316), tridymite (JCPDS Card No. 75–1544) and silicon (JCPDS Card No. 27–1402) peaks due to the preform powders are also detectable. In accordance with the quantitative analysis, the maximum amount of Si_3N_4 is produced under the conditions of trial L_1 (5% NH_3 balance N_2,100 cm^3min^{-1} flow rate, 1300 °C, 90 min) while the minimum amount is achieved in trials $L_{4,5,6,7,8,9}$. In those trials, the silicon nitride peaks at 2θ = 35.33 (210), 20.60 (101), 31.008 (201), could not be detected at 5 wt % and below. It is quite difficult to determine a low Si_3N_4 phase content by any method, since 5 wt % is close to the detection limit of the equipment.

3.3.2. IR absorption spectroscopy

Fig. 6 shows IR-absorption spectra of all test specimens (L1–L9) treated by N_2 precursor and SiF_x (evolved during the decomposition of Na_2SiF_6) at different deposited temperatures.

The infrared absorption spectrum of Si_3N_4 in Fig. 6 shows two broad peaks at about 500 and 1000 cm^{-1} indicating high one-phonon densities of states in these frequency regions [23]. These peaks are most observed in the spectrum of the samples treated under L1,2,3,4 conditions using N_2:NH_3 source at elevated

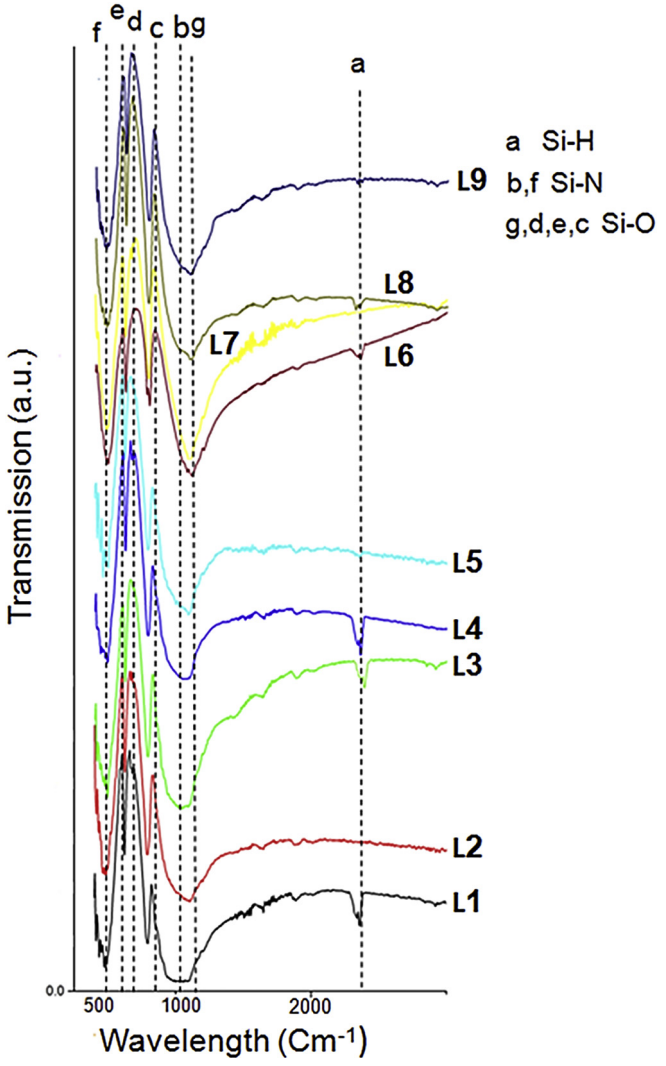

Fig. 6. FT-IR spectrum corresponding to specimens tested under conditions L1-L9. The seven peaks identified are marked from *a* to *g* in the spectra.

temperature (1200 and 1300 °C). The bands from 465 cm^{-1} to 485 cm^{-1} belong to bending vibration of crystalline SiO_2. Also, the bands from 1090 cm^{-1} to 1100 cm^{-1} and from 620 cm^{-1} to 815 cm^{-1} belong to O-Si-O stretching vibrations. In addition, a new peak centered at 800 cm^{-1} corresponding to amorphous SiO_2 is observed in the spectrum of the sample [33]. The absorption due to Si-H (line *a* in the spectra) bonds which has been reported to occur around 2000–2400 cm^{-1} [23] is seen in the samples treated under N_2-NH_3. This can probably be related to reaction of silicon based species with hydrogen produced from decomposition of ammonia and impurity of gas supplier (the gases contain H_2O (g) (<5 ppm)) in higher temperature.

3.4. Microstructural evolution

In sections 3.4.1 and 3.4.2 are discussed two mechanisms that take place in the formation of Si_3N_4.

3.4.1. Solid-gas reactions

There are three possible reaction routes that can be responsible for formation of Si_3N_4 through solid-gas reactions:

The first possible reaction is:

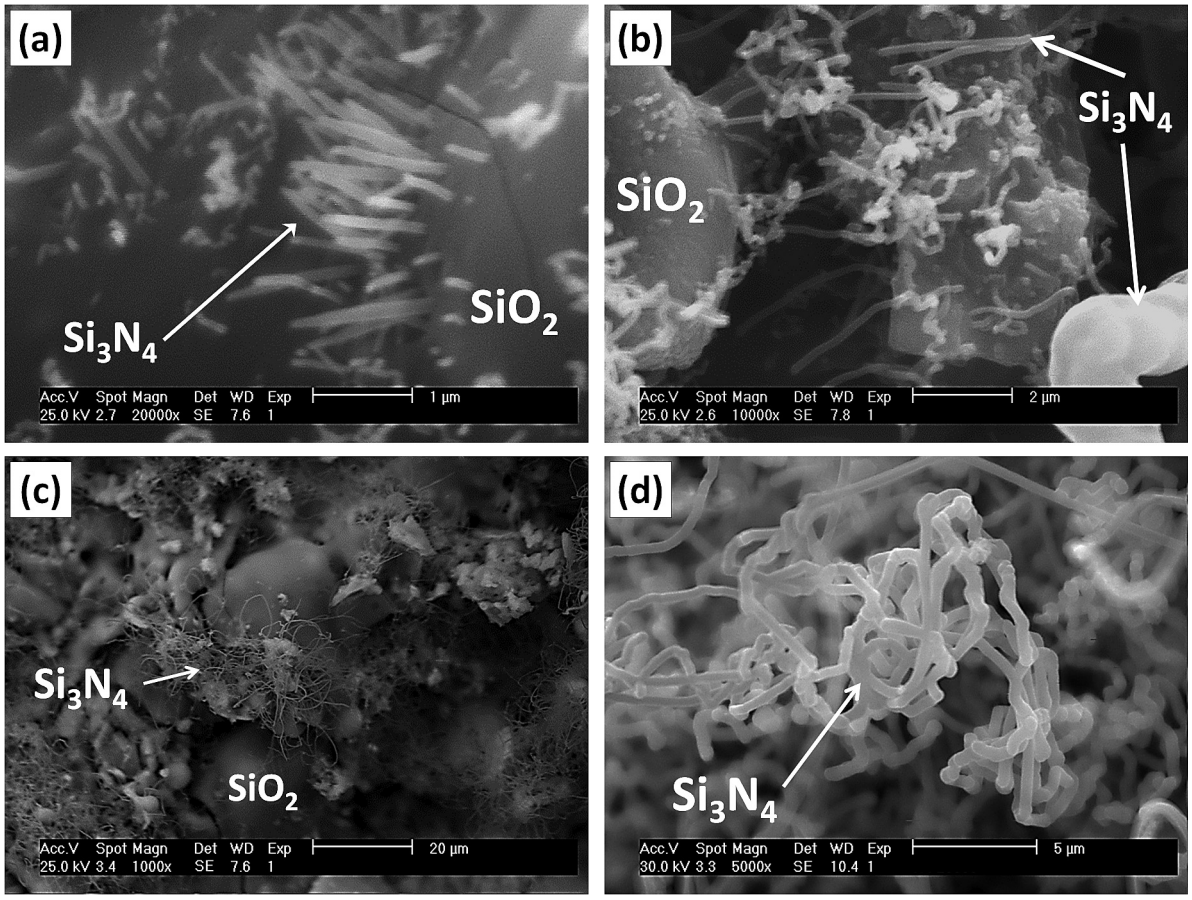

Fig. 7. SEM micrographs showing Si_3N_4 deposited at: a) 1100 °C, N_2-NH_3: 20 cm^3/min, 60 min, b) 1100 °C, N_2-NH_3: 20 cm^3/min, 90 min, c) 1200 °C, N_2-NH_3: 20 cm^3/min, 60 min, and d) 1200 °C, N_2-NH_3: 20 cm^3/min, 90 min.

$$a\,SiFn\,(g) + b\,NH3\,(g) + c\,N2\,(g) = d\,Si3N4\,(s) + n\,HF\,(g) + f\,H2\,(g) \quad \Delta H\,(1300\,^{\circ}C) = -557.3\ kJ/mol \tag{3}$$

(a, b, c, d, n, f are stoichiometric coefficients)

The second possible set of reactions:

$$Si_{(s)} + O_{2\,(g)} = SiO_{(g)} + 0.5O_{2\,(g)} \tag{4}$$

$$Si_{(s)+}\ H_2O_{(g)} = SiO_{(g)} + H_{2\,(g)} \tag{5}$$

$$SiO\,(g) + 0.66NH3\,(g) + 0.33N2\,(g) = 0.33Si3N4\,(s) + H2O\,(g) \quad \Delta H\,(1300\,^{\circ}C) = -382.0\ kJ/mol \tag{6}$$

And the third possible reaction:

$$3Si(g) + 2N_2(g) = Si_3N_4\,(s) \rightarrow \Delta H\,(1300\,^{\circ}C) = -722.0\ kJ/mol \tag{7}$$

Based on thermodynamic predictions, during nitridation, below direct nitridation of solid silicon (<1250 °C) two parallel reactions occur, one involving the nitridation of SiF_n species (reaction (3)), and the other, the nitridation of volatilized silicon and $SiO_{(g)}$ (reactions (4)–(7)). As it can be seen in Fig. 7a the fine needles type of nucleation of Si_3N_4 starts at 1100 °C. By increasing temperature to

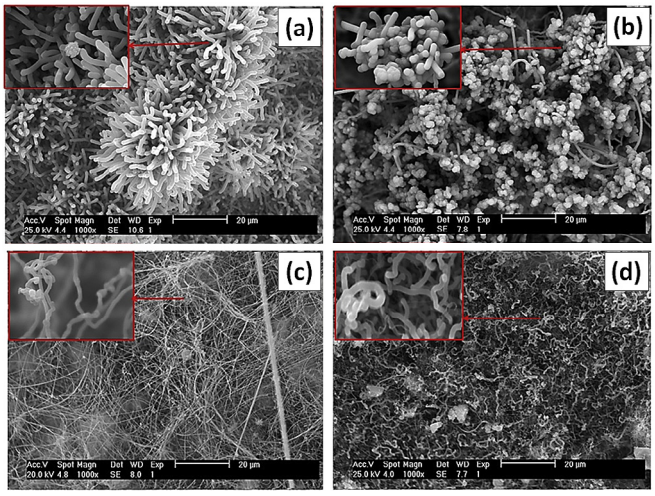

Fig. 8. SEM micrographs showing Si_3N_4 deposited at = 1300 °C and t = 90 min under gas flow rate of: a) 100 cm^3/min, b) 80 cm^3/min, c) 60 cm^3/min, and d) 20 cm^3/min N_2:NH_3.

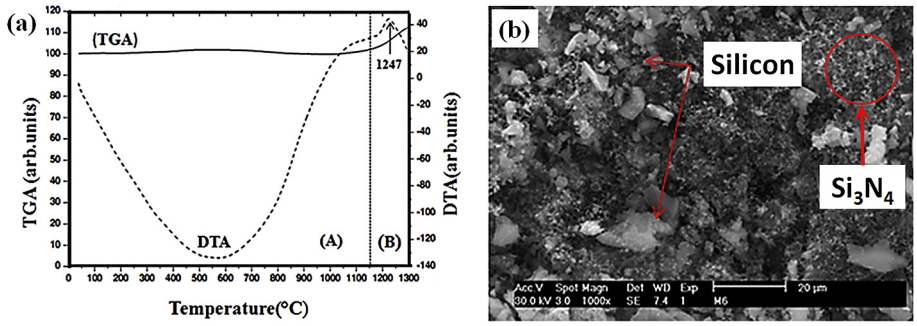

Fig. 9. a) Thermal analysis of silicon by DTA/TG and b) SEM photomicrograph showing Si_3N_4 deposited at 1200 °C, under flow rate of N_2 of 60 cm^3/min for 90 min.

1200 °C silicon nitride is obtained with a wool structure including fine and long fibers (Fig. 7c). With increase in reaction time, Si_3N_4 is obtained with a larger size of fibers and as more compact deposits, especially for samples treated at higher temperature (see Fig. 7(b) and (d)).

At temperature, higher than 1250 °C, direct nitridation (DN) of solid silicon is started. Due to formation of silicon nitride by nitridation of SiF_n at lower temperature (<1300 °C) and also to the more negative Gibbs free energy change of formation of Si_3N_4 by gas phase reaction (reactions (8) and (9)), in comparison to DN of solid silicon (reaction (10)), it is more likely that the gas phase reaction is the leading occurring mechanism.

$$SiF_{4(g)} + SiF_{3(g)} + SiF_{2(g)} + SiF_{(g)} + Si_{(g)} + 6.6NH_{3(g)} = 1.66Si_3N_4 + 10HF_{(g)} + 5H_{2(g)} \quad \Delta G_{1300°C} = -843.2kJ/mol \tag{8}$$

$$SiF_{4(g)} + SiF_{3(g)} + SiF_{2(g)} + SiF_{(g)} + Si_{(g)} + N_{2(g)} + 4.6NH_{3(g)} \rightarrow 1.66Si_3N_4 + 10HF_{(g)} + 2H_{2(g)} \quad \Delta G_{1300°C} = -584.6kJ/mol \tag{9}$$

$$3Si_{(s)} + 2N_{2\,(g)} \rightarrow Si_3N_{4\,(s)} \quad \Delta G_{1300°C} = -154.6kJ/mol \tag{10}$$

Fig. 8 shows scanning electron micrographs of the surface morphology of Si_3N_4 coatings deposited at temperature of 1300 °C under various gas flow rates of N_2:NH_3 [27]. A comparison between average amounts of obtained Si_3N_4 at 1300 °C and 1100–1200 °C by semi-quantitative analysis (XRD) reveals higher formation of silicon nitride at higher process temperatures. Short incubation period of formed Si_3N_4 by direct nitridation of intentionally added silicon at 1300 °C (further discussed in text below) follows a rapid formation and growth of the new phase of Si_3N_4 formed via gas phase reactions of the SiF_x species with the nitrogen precursor. As it can be seen in Fig. 8 by increasing the N_2:NH_3 flow rate from 20 to 100 cm^3/min due to augment of the concentration of reactant, the shape of the formed Si_3N_4 becomes more clearly defined.

As it was mentioned before, thermodynamics shows that Si_3N_4 phase can be obtained by reaction of solid Si with nitrogen at temperature lower than 1250 °C. Fig. 9(a) presents the thermograms (TGA–DTA curves) of a silicon sample. The TGA curve shows just one stage of gain weight (B stage). At B stage (1150–1300 °C, gain weight = 10%), one exothermic peak at 1247 °C in the DTA curve, which comes from the nitridation of Si was observed. Therefore, at temperatures higher than 1247 °C the direct nitridation of silicon, besides the vapor phase reaction is expected. Fig. 9(b) shows that Si particles remained intact at temperature less than 1250 °C.

The highly exothermic reaction between SiF_n species and NH_3 at higher temperature and gas flow rate induces large supersaturation of Si atoms and the active nitrogen atoms on the surface of small primary Si_3N_4. This is due to the fact that by increase in gas flow rate, the concentration of reactants increases (higher supersaturation), accordingly. At flow rates of 20 and 60 cm^3/min due to low supersaturation, just fine long fibers in their particular orientations can be observed. However, as the supersaturation is increased, the nucleation rate of other orientations becomes sufficiently greater than those under lower gas flow rates. Therefore, it causes fast alteration into rod-like Si_3N_4 crystals, i.e. the initial Si_3N_4 stem on the primary Si_3N_4. As long as these growing parameters are satisfied at the tip of the stem, the stems grow.

The observed dendrite structure usually results from rapid crystallization at large supersaturation stages [34]. The alternate aggregation and consumption of reactant atoms at the front of the growth interface give rise to the fluctuation of supersaturation around the stems, and further to the formation of bulges on the surface of stems. The bulges are generated preferentially at the sites with higher supersaturation. It is known that latent heat is released more quickly at these tips [35], resulting in a higher temperature at the growth front, the rapid reaction of Si and N atoms, the higher growth rate at the tips, and finally the formation of Si_3N_4 dendrites (see Fig. 10).

By increasing temperature, the interaction between N_2-NH_3 and SiF_n is not the only dominant reaction. Based on the literature it should be noted that at ~1300 °C, the fastest nitridation rate can readily account for the reaction of evaporated silicon with nitrogen [36]. The silicon present in the substrate that partially is converted to the gas phase, not only increases the partial pressure of SiF_2 and SiF_3 reactive gases through reactions of (1) and (2) in the system, but also interacts with oxygen present in the system. The formation of silicon nitride by the help of oxygen is well documented [37,38]. The presence of trivial amounts of oxygen or water in the system can have a dramatic effect on increasing the weight percentage of silicon nitride phase in the final product.

It was reported that the presence of H_2O and oxygen can accelerate formation of silicon nitride by generation of SiO that it is confirmed by weight loss of silicon during thermogravimetric analysis tests and by the presence of small amount of these gases

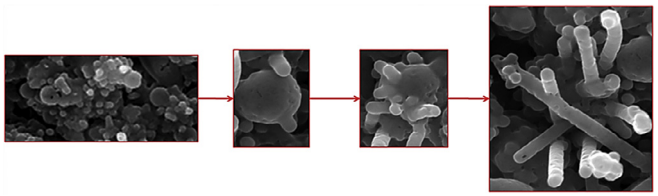

Fig. 10. SEM micrograph illustrating the growth stages of Si_3N_4 dendrites at 1300 °C.

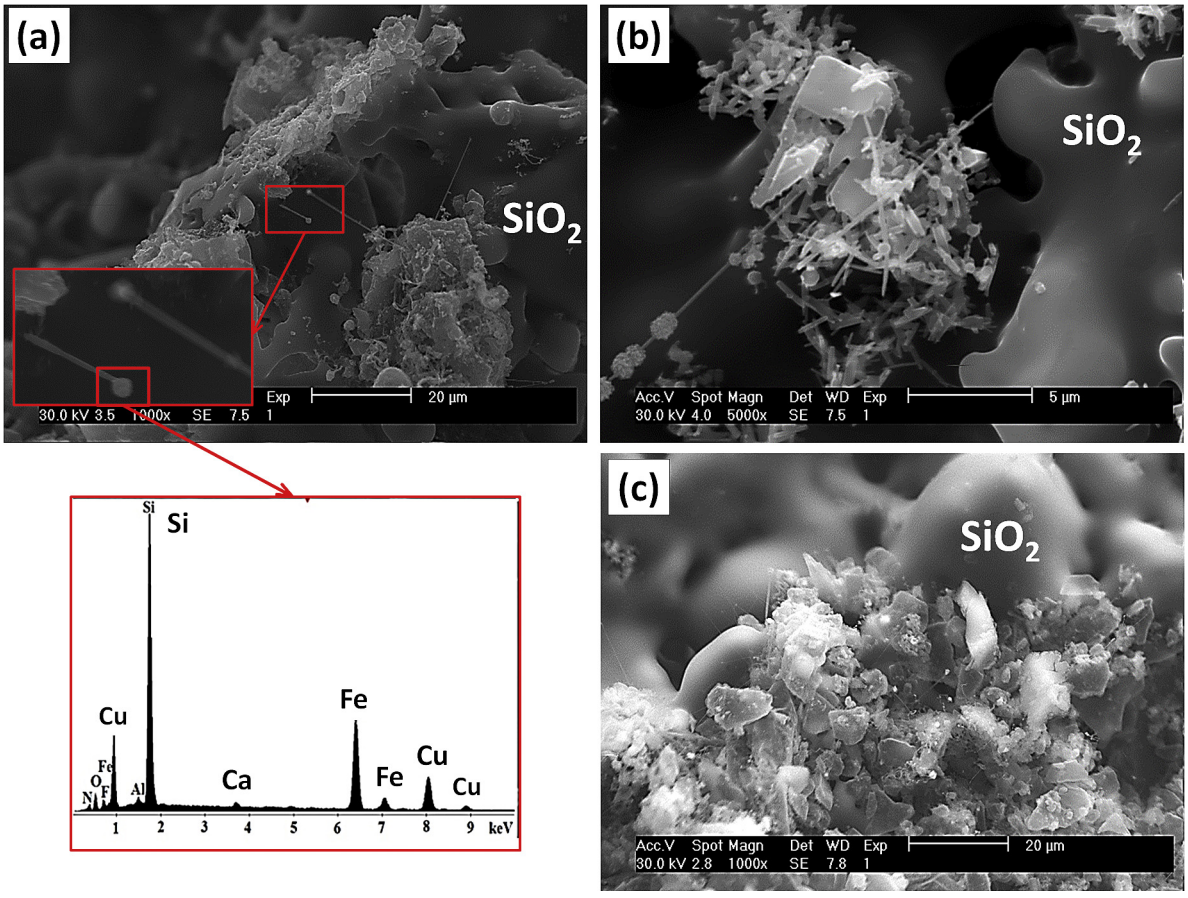

Fig. 11. SEM micrographs showing Si_3N_4 deposited at a) and b) 1100 °C, N_2-NH_3: 60 cm^3/min, 45 min, and c) 1100 °C, N_2:60 cm^3/min, 45 min.

[39]. The nitridation of SiO and SiF_4 can also be assisted by the parallel formation of H_2, released from dissociation of H_2O.

3.4.2. Vapor liquid solid (VLS) mechanism

In this mechanism, small liquid droplets do act as preferred sites for whisker growth and Si_3N_4 growth can be induced by catalysts originated from metallic impurities in rice husk. Upon heating, the catalysts decompose, and the metallic silicides in the form of liquid eutectic droplets are formed which can dissolve the reactant gases until reaching a supersaturated state. From EDS analysis of the bright part, the presence of iron impurity and silicon were confirmed. Fe_2O_3 is easily reduced under low hydrogen partial pressure to the metal, which in turn yields the liquid silicides at the nitridation temperature [40]. Thanks to the ability of Fe in reducing the melting temperature of silicon up to 200 °C, Fe-Si alloy (with low melting point) as the catalyst can impose one dimensional anisotropic growth. Due to the low solubility of nitrogen in the liquid phase (Fe-Si) that is confirmed by EDS result, nitridation of silicon must occur at the solid-liquid interface to lengthen the needle. As it can be seen from Fig. 11, a small amount of very fine whiskers of Si_3N_4 was observed at 1100 °C due to closeness of this temperature to the lowest eutectic temperature of the Fe-Si system. As it can be observed in Fig. 11(a), (b) and (c), due to the higher reactivity of NH_3 than that of N_2, the diameter of whiskers in the presence of N_2 is smaller than in the mixture N_2-NH_3. N_2 is thermally and chemically more stable than ammonia, which explains its difficult dissociation to lower molecular weight species (ionization potentials for N_2 and NH_3 are 15.576 and 10.2 eV, respectively) [41]. Also, the ease of dissociation of NH_3 may be related to the low strength N-H bond (1315 kJ mol^{-1}) if compared with the N-N bond (3977 kJ mol^{-1}) at 25 °C, which make NH_3 a more suitable precursor than N_2 in system [42].

After nucleation of thin whiskers by a VLS mechanism, direct reaction of SiF_n species and NH_3-N_2 mixture on the surface of the whiskers could be counted as a second stage to thicken the whiskers. The thinner stem of whiskers in Fig. 11(c) shows that the rate of the second stage is low in the presence of N_2.

Due to the high surface reactivity and absorptivity of the stem, Fe atoms in the vicinity around the whiskers can be absorbed on the surface and play the role of new nucleation centers to develop new whiskers on the side of the original one, leading to the formation of Si_3N_4 branches. Fig. 11(b) shows the morphology of the tip from which another whisker has grown. The whiskers grown secondarily from the droplet are formed by a bottom VLS mechanism. Besides multi-ball-like droplets were observed in Fig. 11(b); this kind of structures were rarely observed on the tip.

3.5. Optimization of process parameter

With the aim of determining the percent contribution of each of the parameters tested to the variability in the amount of Si_3N_4 formed, an analysis of variance (ANOVA) was performed. As shown in Table 2, results from the ANOVA reveal that the parameter that most significantly influences the variability in the amount of deposited phase is processing temperature, followed by type of gas and processing time, with relative contributions of 59, 21 and 12%, respectively. The percent contribution due to the error term provides an estimate of the adequacy of the experiment. In this case,

Table 2
ANOVA table for weight percentage of Si_3N_4.

Column	Factor	F[a]	S[b]	V[c]	P[d]
1	Temperature (A)	2	80.2	40.32	59
2	Time (B)	2	16.1	8.05	12
3	Type of gas (C)	2	28.5	14.285	21
4	Gas flow rate (D)	1	8.06	4.44	6
5	Error	10	1.035	0.0325	2
	Total	17	134.36		100

[a] Degrees of freedom: DOF.
[b] Sum of squares.
[c] Variance.
[d] Percentage contribution.

the low magnitude of the error term (2%) suggests that no important factors were omitted in the design of the experiment, and that no measurement errors were insignificant.

Fig. 12 shows the main effects of the level average responses for parameters on Si_3N_4 formation. It can be concluded that according to the maximizing criterion that 'the larger the better', $A_1B_1C_1D_1$ are the best conditions for maximum amount of Si_3N_4. Therefore, the optimum conditions to promote and maximize the selective formation of Si_3N_4 are as follows: 1300 °C for 90 min and N_2-5% NH_3 as nitrogen precursor at a gas flow rate of 100 cm^3/min, as shown in Table 2.

Cracks in preforms and non-uniformity of particles can be generated during preform fabrication and/or infiltration process. Therefore, the preforms should be made sound and without any cracks to the extent possible. Fig. 13 shows the three-dimensional image of RHA preforms before and after CVI process. As a rule, materials possessing higher density (ρ) or high atomic number (Z) tend to better absorb X-rays. The relationship is best expressed in the formula for X-ray absorption coefficient (μ):

$$\mu \approx \frac{\rho Z^4}{AE^3} \tag{11}$$

where A is the atomic mass and E is the X-ray energy. The strong relationship between absorption and atomic number is of significant importance in many materials characterization and clinical applications. The Z^4 factor allows for contrast levels of several orders of magnitude between different materials [43–45].

As it can be observed from Fig. 13(a), the preform is crack free and the porosities are distributed uniformly through the preform. Fig. 13(b) illustrates the preform after CVI process. Due to higher density and molecular weight of Si_3N_4, the preform appears in lighter shade in comparison to the preform before CVI process (Fig. 13(a)). The bright spots in Fig. 13(b) could correspond to the agglomeration of Si_3N_4 fibers in the spaces between RHA particles. No defects in the scale of higher than 5 mm, such as microcracks are

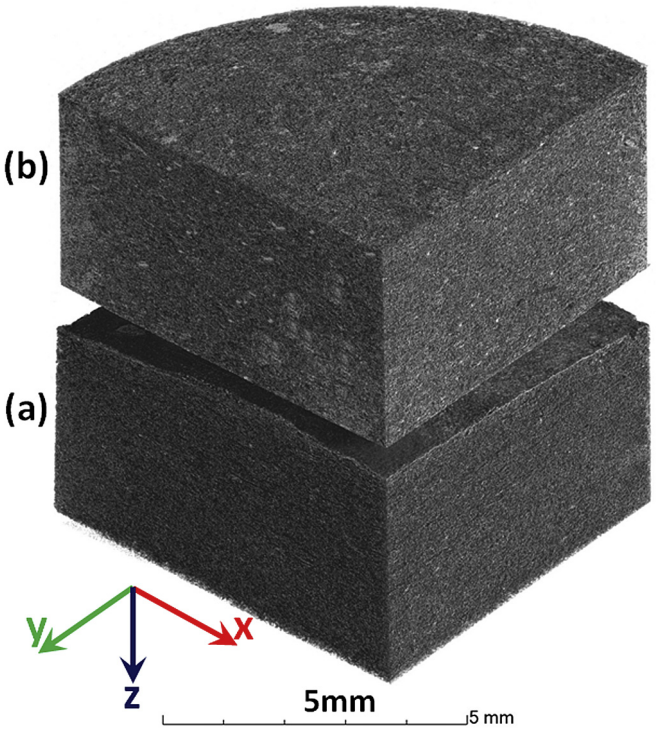

Fig. 13. A 3D tomographic image of RHA preforms, a) before, and b) after CVI process.

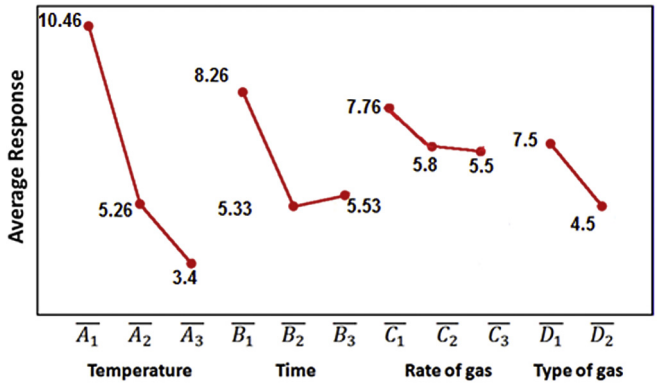

Fig. 12. Graph of the main effects of the level average responses for process parameters on Si_3N_4 formation.

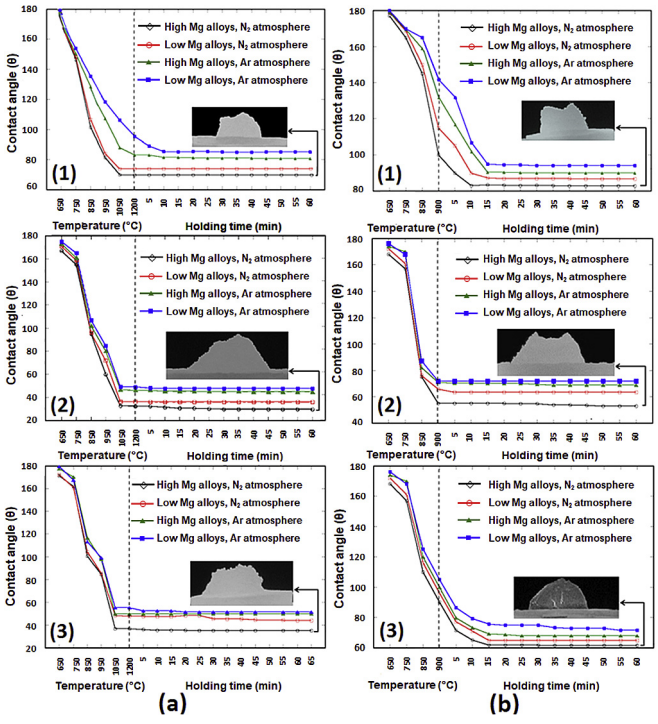

Fig. 14. Variation of contact angle (θ) as a function of time during isothermal period at temperatures of: a) 900 and b) 1200 °C on 1) silica, 2) Si_3N_4 and 3) coated silica substrate, performed in nitrogen atmosphere.

found in the inner structure of the preform.

3.6. Wettability behavior of RHA, RHA/Si_3N_4 and Si_3N_4 substrates

Graphs of contact angle changes with time at 900 and 1200 °C are shown in Fig. 14. The curves in Fig. 14(a, b and c) show three ranges of behavior. In the first range, the contact angle is constant. This range of contact angle is typical in aluminum droplets which are covered with a thin alumina film preventing a real contact between the molten aluminum and ceramic substrates [46]. In the second part of the curves, dramatic decrease in contact angle were observed. As it is clear from Fig. 14, due to melting of the alloys there is a sharp increment in the diameter of droplet in all the conditions in comparison to the primary size of alloy droplet, but depends on the chemical composition of the alloy and substrate and the presence of the obstructions of the cracks and small cavities in the substrate, this gradient can be soft or sharp. In the third part of the curves the droplet size, contact angle and work of adhesion remain constant.

In Al-SiO_2 system, a gradual decrease in the contact angles was observed as temperature increases and no sharp transition from non-wetting ($\theta = 90°$) to wetting behavior was observed at T = 900 and 1200 °C under nitrogen atmosphere. At 900 °C, the angle changed continuously until it reached to constant degree after 10–15 min. However, at 1200 °C, the contact angle remains constant immediately without any interval time. The contact angle is still non-wettable under Ar atmosphere at temperature of 900 °C. The decrease in contact angle indicates that the progress in wettability between Al and SiO_2 substrate can occur in the presence of both Mg and N_2. Saravanan et al. [47], reported that the surface tension of Al in N_2 was greatly reduced compared to the values obtained in Ar at temperatures higher than 850 °C, but this effect was still too weak to improve the wettability unless enhanced by alloying additions. By alloying the aluminum, the free energy of the solid contact with a liquid -Δg^{sl} increases due to formation of interfacial reaction of $MgAl_2O_4$, MgO (reaction (12)–(14)) that helps to improve the wettability.

$$2Mg(l) + SiO_2(s) = 2MgO(s) + Si(s) \quad \Delta G^\circ (1200\ ^\circ C) = -267\ kJ/mol \tag{12}$$

$$Mg(l) + 2SiO_2(s) + 2Al(l) = MgAl_2O_4(s) + 2Si(s) \quad \Delta G^\circ (1200\ ^\circ C) = -379\ kJ/mol \tag{13}$$

$$2MgO(s) + 3SiO_2(s) + 4Al(l) = 2MgAl_2O_4(s) + 3Si(s) \quad \Delta G^\circ (1200\ ^\circ C) = -466\ kJ/mol \tag{14}$$

The difference of contact angles at 1200 °C under two different atmospheres, can be explained by this scenario that in the nitrogen atmosphere in addition to abovementioned reactions, the MgO and $MgAl_2O_4$ phases are created by the reaction of Mg_3N_2 (reaction (15)) with oxygen. As it can be seen from reaction (16) and (17), thermodynamically formation of MgO and $MgAl_2O_4$ is more favorable under nitrogen atmosphere due to the lower Gibbs energy compared to argon.

$$3Mg(l) + N_2(g) = Mg_3N_2(g) \quad \Delta G^\circ (1200\ ^\circ C) = -147\ kJ/mol \tag{15}$$

$$Mg_3N_2(g) + 1.5\ O_2(g) = 3\ MgO(s) + N_2(g) \quad \Delta G^\circ (1200\ ^\circ C) = -117\ kJ/mol \tag{16}$$

$$Mg_3N_2(g) + 6O_2(g) + 6Al(l) = 3MgAl_2O_4(s) + N_2(g) \quad \Delta G^\circ (1200\ ^\circ C) = -4939\ kJ/mol \tag{17}$$

In Al-Si_3N_4, in comparison to Al-SiO_2 system a dramatic decrease in the contact angles was observed as temperature increases and sharp transition from non-wetting ($\theta = 90°$) to wetting behavior was observed at T = 900 °C, under nitrogen atmosphere and T = 1200 °C for all experimental levels. It shows the time independence of the contact angle for wetting in Si_3N_4 particulates with liquid aluminum alloys in an isothermal part. This improvement in the wetting in comparison to silica system can be due to formation of AlN. Good bonding between the AlN and Al has been reported in various investigations [48,49].

Formation of AlN depends on a direct nitridation of aluminum (reaction (18)) or two-step reaction: reaction of Mg and N_2 to form Mg_3N_2 and then formation of AlN by reaction of Mg_3N_2 and Al (reaction (15) and (19)). The lower Gibbs free energy summation of reactions (15) and (19) with value of −346 kJ/mol shows that magnesium nitride helps in promoting formation of AlN [49,50]:

$$2Al(l) + N_2(g) = 2AlN(s) \quad \Delta G^\circ (1200\ ^\circ C) = -312\ kJ/mol \tag{18}$$

$$Mg_3N_2(g) + 2Al(l) = 2AlN(s) + 3Mg(l) \quad \Delta G^\circ (1200\ ^\circ C) = -199\ kJ/mol \tag{19}$$

By CVD coating of silica, a significant reduction in the contact angles was observed with increasing temperature. A sudden decrease in contact angle from non-wetting ($\theta \geq 90°$) to wetting behavior was observed at 1200 °C under nitrogen atmosphere for alloy with high Mg content. The improvement of contact angle in comparison to SiO_2/Al alloy system shows that the coatings applied to silica improved its wettability by aluminum alloy.

4. Conclusions

Based on the results and discussion, within the framework of the experimental design, in the range of parameters and levels established for this study, it can be concluded that:

1. Results from the analysis of variance (ANOVA) show that the parameter that most significantly impacts the variability in the total amount of Si_3N_4 deposited, is processing temperature (59% contribution), followed by the type of gas (21%), processing time (12%) and finally, gas flow rate (6%).

2. The optimal processing parameters to maximize the amount of silicon nitride deposited on RHA are: at 1300 °C for 90 min, in N_2- 5% NH_3 at a flow rate of 100 cm^3/min.
3. The morphology of Si_3N_4 depends significantly upon reaction conditions, being temperature the parameter that plays the main role. In the presence of nitrogen, the morphology of the products ranges from fine, wool-like fibers and spongy deposits to more compact deposits.
4. Below 1300 °C, regardless the amount of SiF_n and N_2-5% NH_3 and time, Si_3N_4 particles and dendrites can hardly be obtained except with the morphology of fine fibers or wool like shape.
5. At 1300 °C, the nucleation and growth of Si_3N_4 increases. At the lower test temperatures, fewer Si_3N_4 nuclei are generated possibly due to the lower reaction rate. Moreover, at 1300 °C direct nitridation also operates, resulting in the creation of primary nuclei of Si_3N_4. As long as supersaturation of the gas surrounding the nuclei and temperature are high enough, the growth of dendrites is promoted mainly because of the exothermic reaction for Si_3N_4 formation.
6. The minimum contact angles obtained with high Mg content in alloy at 1200 °C and nitrogen atmosphere in Si_3N_4, SiO_2 and Si_3N_4-coated RHA substrates, are 30°, 72° and 35°, respectively, suggesting the beneficial effect of coating RHA with Si_3N_4 by HYSY-CVI.

Acknowledgments

Ms. Niloofar Soltani and Mr. Amin Bahrami gratefully acknowledge DGAPA-UNAM and CONACyT for granting a postdoctoral and doctoral scholarship, respectively. The authors are also thankful to Cinvestav IPN-Saltillo for support in the research activities in the field of advanced materials. The authors also thank Mr. Paul Kamm for his help during laser microtomography analyses.

References

[1] F. Brunk, Silica refractories, CN Refractories(Germany) 5 (2001) 27–30.
[2] S. Sutton (Ed.), Ceramic Components Directory, Ceramic Industry, 2011.
[3] A. Bahrami, M.I. Pech-Canul, N. Soltani, C.A. Gutiérrez, P.H. Kamm, A. Gurlo, Tailoring microstructure and properties of bilayer-graded Al/B_4C/$MgAl_2O_4$ composites by single-stage pressureless infiltration, J. Alloys Compd. 694 (2017) 408–418.
[4] A. Bahrami, N. Soltani, S. Soltani, M.I. Pech-Canul, L.A. Gonzalez, C.A. Gutierrez, A. Möller, J. Tapp, A. Gurlo, Mechanical, thermal and electrical properties of monolayer and bilayer graded Al/SiC/rice husk ash (RHA) composite, J. Alloys Compd. 699 (2017) 308–322.
[5] J.A.K. Gladston, N.M. Sheriff, I. Dinaharan, J.D. Raja Selvam, Production and characterization of rich husk ash particulate reinforced AA6061 aluminum alloy composites by compocasting, Trans. Nonferrous Metals Soc. China 25 (2015) 683–691.
[6] N. Soltani, U. Simon, A. Bahrami, X. Wang, S. Selve, J.D. Epping, M.I. Pech-Canul, M.F. Bekheet, A. Gurlo, Macroporous polymer-derived SiO_2/SiOC monoliths freeze-cast from polysiloxane and amorphous silica derived from rice husk, J. Eur. Ceram. Soc. 37 (2017) 4809–4820.
[7] I. Dinaharan, K. Kalaiselvan, N. Murugan, Influence of rice husk ash particles on microstructure and tensile behavior of AA6061 aluminum matrix composites produced using friction stir processing, Compos. Commun. 3 (2017) 42–46.
[8] A. Bahrami, U. Simon, N. Soltani, S. Zavareh, J. Schmidt, M.I. Pech-Canul, A. Gurlo, Eco-fabrication of hierarchical porous silica monoliths by ice-templating of rice husk ash, Green Chem. 19 (2017) 188–195.
[9] A. Bahrami, M.I. Pech-Canul, C.A. Gutiérrez, N. Soltani, Wetting and reaction characteristics of crystalline and amorphous SiO_2 derived rice-husk ash and SiO_2/SiC substrates with Al–Si–Mg alloys, Appl. Surf. Sci. 357 (Part A) (2015) 1104–1113.
[10] A. Bahrami, N. Soltani, M.I. Pech-Canul, C.A. Gutiérrez, Development of metal-matrix composites from industrial/agricultural waste materials and their derivatives, Crit. Rev. Environ. Sci. Technol. 46 (2016) 143–208.
[11] N. Soltani, S. Soltani, A. Bahrami, M.I. Pech-Canul, L.A. Gonzalez, A. Möller, J. Tapp, A. Gurlo, Electrical and thermomechanical properties of CVI- Si_3N_4 porous rice husk ash infiltrated by Al-Mg-Si alloys, J. Alloys Compd. 696 (2017) 856–868.
[12] M. Naka, Aluminum/ceramic interface structure and its related properties, Ultramicroscopy 39 (1991) 128–134.
[13] M. Wang, M. Xie, L. Ferraioli, Z. Yuan, D. Li, D. Yang, L. Pavesi, Light emission properties and mechanism of low-temperature prepared amorphous SiN films. I. Room-temperature band tail states photoluminescence, J. Appl. Phys. 104 (2008) 083504.
[14] M. Herrmann, H. Klemm, C. Schubert, Silicon Nitride Based Hard Materials, Handbook of Ceramic Hard Materials, 2000, pp. 749–801.
[15] H.M. Jennings, B.J. Dalgleish, P. Pratt, Reactions between silicon and nitrogen, J. Mater. Sci. 23 (1988) 2573–2583.
[16] S.J. Durham, K. Shanker, R.A. Drew, Carbothermal synthesis of silicon nitride: effect of reaction conditions, J. Am. Ceram. Soc. 74 (1991) 31–37.
[17] G. Ziegenbalg, U. Breuel, E. Ebrecht, H. Holldorf, R. Brink, Synthesis of α-silicon nitride powder by gas-phase ammonolysis of CH_3SiCl_3, J. Eur. Ceram. Soc. 21 (2001) 947–958.
[18] E. Kroke, M. Schwarz, Novel group 14 nitrides, Coord. Chem. Rev. 248 (2004) 493–532.
[19] N. Soltani, A. Bahrami, M.I. Pech-Canul, L.A. González, Review on the physicochemical treatments of rice husk for production of advanced materials, Chem. Eng. J. 264 (2015) 899–935.
[20] R. Livengood, D. Hess, Electrical properties of plasma-deposited fluorinated silicon nitride, Thin solid films 162 (1988) 59–65.
[21] O. Sanchez, C. Gomez-Aleixandre, M. Fernandez, J. Albella, Influence on the electrical characteristics of the-NH radicals incorporated into PECVD silicon nitride films, Vacuum 39 (1989) 727–729.
[22] C.P. Chang, D.L. Flamm, D.E. Ibbotson, J.A. Mucha, Fluorinated chemistry for high-quality, low hydrogen plasma-deposited silicon nitride films, J. Appl. Phys. 62 (1987) 1406–1415.
[23] S. Fujita, H. Toyoshima, T. Ohishi, A. Sasaki, Plasma-deposited silicon nitride films from SiF 2 as silicon source, Jpn. J. Appl. Phys. 23 (1984) L268–L270.
[24] C. Morosanu, E. Segal, A comparison of kinetic parameters for various CVD-Si_3N_4 films, Mater. Chem. 7 (1982) 79–87.
[25] N. Soltani, A. Bahrami, M.I. Pech-Canul, L.A. González, A. Gurlo, Kinetics of silicon nitride formation on SiO_2-derived rice husk ash using the chemical vapor infiltration method, Int. J. Chem. Kinet. 49 (2017) 293–302.
[26] A. Bahrami, M.I. Pech-Canul, C.A. Gutierrez, N. Soltani, Effect of rice-husk ash on properties of laminated and functionally graded Al/SiC composites by one-step pressureless infiltration, J. Alloys Compd. 644 (2015) 256–266.
[27] N. Soltani, A. Bahrami, M. Pech-Canul, L. González, A. Gurlo, Kinetics of silicon nitride formation on SiO_2-derived rice husk ash using the chemical vapor infiltration method, Int. J. Chem. Kinet. 49 (2017) 293–302.
[28] N. Soltani, M.I. Pech-Canul, L.A. González, A. Bahrami, Mechanism and parameters controlling the decomposition kinetics of Na_2SiF_6 powder to SiF_4, Int. J. Chem. Kinet. 48 (2016) 379–395.
[29] S. Fujita, T. Ohishi, H. Toyoshima, A. Sasaki, Electrical properties of silicon nitride films plasma-deposited from SiF_4, N_2, and H_2 source gases, J. Appl. Phys. 57 (1985) 426–431.
[30] M. Weber, P. Armentrout, Energetics and dynamics in the reaction of Si with SiF. Thermochemistry of SiF and SiF (x= 1, 2, 3), J. Chem. Phys. 88 (1988) 6898.
[31] M. Farber, R. Srivastava, Mass spectrometric determination of the heats of formation of the silicon fluorides SiF(g), SiF_2(g) and SiF_3(g), J. Chem. Soc. Faraday Trans. 1 Phys. Chem. Condens. Phases 74 (1978) 1089–1095.
[32] R.A. King, V.S. Mastryukov, H.F. Schaefer III, The electron affinities of the silicon fluorides SiFn (n= 1–5), J. Chem. Phys. 105 (1996) 6880–6886.
[33] P.J. Launer, Infrared Analysis of Organosilicon Compounds: Spectra-structure Correlations, Silicone Compounds Register and Review, 1987, pp. 100–103.
[34] H. Yan, R. He, J. Johnson, M. Law, R.J. Saykally, P. Yang, Dendritic nanowire ultraviolet laser array, J. Am. Chem. Soc. 125 (2003) 4728–4729.
[35] G. Eising, B.J. Niebuur, A. Pauza, B.J. Kooi, Competing crystal growth in Ge–Sb phase-change films, Adv. Funct. Mater. 24 (2014) 1687–1694.
[36] P. Longland, A. Moulson, The growth of α-and β-Si_3N_4 accompanying the nitriding of silicon powder compacts, J. Mater. Sci. 13 (1978) 2279–2280.
[37] D. Messier, P. Wong, A. Ingram, Effect of oxygen impurities on the nitridation of high-purity silicon, J. Am. Ceram. Soc. 56 (1973) 171–172.
[38] J. Torre, A. Mocellin, Some effects of Al and O2 on the nitridation of silicon compacts, J. Mater. Sci. 11 (1976) 1725–1733.
[39] D.R. Messier, P. Wong, Kinetics of nitridation of Si powder compacts, J. Am. Ceram. Soc. 56 (1973) 480–485.
[40] O. Wimmers, P. Arnoldy, J. Moulijn, Determination of the reduction mechanism by temperature-programmed reduction: application to small iron oxide (Fe_2O_3) particles, J. Phys. Chem. 90 (1986) 1331–1337.
[41] J.M. Blocher Jr., Structure/property/process relationships in chemical vapor deposition CVD, J. Vac. Sci. Technol. 11 (1974) 680–686.
[42] R. Weast, G. Tove, Handbook of Chemistry and Physics, The Chemical Rubber Co, Publisher, Cleveland, 1970.
[43] H. Lusic, M.W. Grinstaff, X-ray-computed tomography contrast agents, Chem. Rev. 113 (2013) 1641–1666.
[44] F. García Moreno, M. Fromme, J. Banhart, Real-time x-ray radioscopy on metallic foams using a compact micro-focus source, Adv. Eng. Mater. 6 (2004) 416–420.
[45] S. Poncsák, L. Kiss, R. St-Pierre, S. Guérard, J.F. Bilodeau, Structural Characterisation and Thermophysical Properties of the Side Ledge in Hall-héroult Cells, Light Metals 2014, John Wiley & Sons, Inc, 2014, pp. 585–589.
[46] V. Laurent, D. Chatain, N. Eustathopoulos, European materials research society 1990 spring meeting on metal matrix composites wettability of SiO2 and oxidized SiC by aluminium, Mater. Sci. Eng. A 135 (1991) 89–94.
[47] R. Saravanan, J. Molina, J. Narciso, C. Garcıa-Cordovilla, E. Louis, Effects of

nitrogen on the surface tension of pure aluminium at high temperatures, Scr. Mater. 44 (2001) 965–970.
[48] J. Liu, J. Binner, R. Higginson, Z. Zhou, Interfacial reactions and wetting in Al–Mg/oxide ceramic interpenetrating composites made by a pressureless infiltration technique, Compos. Sci. Technol. 72 (2012) 886–893.
[49] M.I. Pech-Canul, R.N. Katz, M.M. Makhlouf, Optimum parameters for wetting silicon carbide by aluminum alloys, Metallurgical Mater. Trans. A 31 (2000) 565–573.
[50] M.I. Pech-Canul, R.N. Katz, M.M. Makhlouf, S. Pickard, The role of silicon in wetting and pressureless infiltration of SiCp preforms by aluminum alloys, J. Mater. Sci. 35 (2000) 2167–2173.